# REPORT DOCUMENTATION PAGE

Form Approved
OMB No. 0704-0188

Public reporting burden for this collection of information is estimated to average 1 hour per response, including the time for reviewing instructions, searching data sources, gathering and maintaining the data needed, and completing and reviewing the collection of information. Send comments regarding this burden estimate or any other aspect of this collection of information, including suggestions for reducing this burden to Washington Headquarters Service, Directorate for Information Operations and Reports, 1215 Jefferson Davis Highway, Suite 1204, Arlington, VA 22202-4302, and to the Office of Management and Budget, Paperwork Reduction Project (0704-0188) Washington, DC 20503.

**PLEASE DO NOT RETURN YOUR FORM TO THE ABOVE ADDRESS.**

| 1. REPORT DATE (DD-MM-YYYY) | 2. REPORT DATE | 3. DATES COVERED (From - To) |
|---|---|---|
| 08/23/07 | Final Report | 06/01/03-02/28/07 |

**4. TITLE AND SUBTITLE**

AFOSR Final Report - Controlled Precipitation of Radiation Belt Particles

**5a. CONTRACT NUMBER**

**5b. GRANT NUMBER**
F49620-03-1-0338

**5c. PROGRAM ELEMENT NUMBER**

**6. AUTHOR(S)**

Inan, Umran, S., Bell, Timothy, F., Chevalier, Timothy, W.

**5d. PROJECT NUMBER**

**5e. TASK NUMBER**

**5f. WORK UNIT NUMBER**

**7. PERFORMING ORGANIZATION NAME(S) AND ADDRESS(ES)**

STAR Laboratory, Packard Building
Stanford University
Stanford, CA 94305

**8. PERFORMING ORGANIZATION REPORT NUMBER**

**9. SPONSORING/MONITORING AGENCY NAME(S) AND ADDRESS(ES)**

Department of the Air Force NE
Air Force Office of Scientific Research
875 N. Randolph St., Suite 325, Room 3112
Arlington, Virginia 22203-1768

**10. SPONSOR/MONITOR'S ACRONYM(S)**

AFOSR/PKR2

**11. SPONSORING/MONITORING AGENCY REPORT NUMBER**

**12. DISTRIBUTION AVAILABILITY STATEMENT**

Distribution Statement A: unlimited   AFRL-SR-AR-TR-07-0350

**13. SUPPLEMENTARY NOTES**

**14. ABSTRACT**

on separate sheet

**15. SUBJECT TERMS**

Simulation of antennas in magnetized plasmas, simulation of waves in magnetized plasmas, absorbing boundary conditions

| 16. SECURITY CLASSIFICATION OF: | | | 17. LIMITATION OF ABSTRACT | 18. NUMBER OF PAGES | 19a. NAME OF RESPONSIBLE PERSON |
|---|---|---|---|---|---|
| a. REPORT | b. ABSTRACT | c. THIS PAGE | | | |
| | | | | | 19b. TELEPONE NUMBER (Include area code) |

Standard Form 298 (Rev. 8-98)
Prescribed by ANSI-Std Z39-18

This work constitutes a major achievement in the determination of the coupling behavior of antennas to a magnetoplasma using a multi step approach. The cold plasma model was the simplest approximation used and from the results we were able to obtain some insight into the coupling of dipole antennas to the surrounding plasma. From the cold plasma simulation results, we determined that the current distribution was triangular for the antenna parameters used which validates the assumption used in previous analytical work. Also, in the absence of the sheath, it was shown that for frequencies above the LHR frequency, the input impedance does not vary significantly as a function of frequency meaning that the antenna is self tuning and can be used over a broad frequency range. With the addition of the warm plasma fluid approximation, we gained the capability of examining the formation of the electrostatic sheath and were able to draw a number of conclusions based on these results. The first result is that sheath structure is periodic using a sinusoidal waveform excitation exhibiting a quasi-steady state structure. In addition, we have shown that the common assumption of immobile protons used in past work is incorrect with the density of protons varying significantly throughout the sheath region and contributing slightly to the current collection. Lastly, we have shown that not only does the sheath dominate the tuning properties of the antenna, but that the time-varying resistance and capacitance throughout the RF cycle do not vary by orders of magnitude (logarithmically) as suggested by previous authors [Miodnosky and Garriott, 1963, Baker et al., 1973, Song et al., 2007].

# AFOSR Final Report

June 1, 2003 - February 28, 2007
STAR Laboratory, Dept. of Electrical Engineering
Stanford University

20070920026

# Final Report to the Air Force Office of Scientific Research

**Principal Investigator**: Professor Umran S. Inan

**Mailing Address:** Space, Telecommunications and Radioscience (STAR) Laboratory
Packard Bldg. Room 355, 350 Serra Mall
Stanford University, Stanford, CA 94305-9515

**Email Address:** inan@nova.stanford.edu

# ResearchObjectives

The overall objectives of this work are to:

- Quantify the requirements for controlled precipitation of radiation belt particles in order to mitigate space particle effects
- Address the issue of coupling of space based antennas to the surrounding magnetoplasma for use in system design
- Determine radiated power from single transmitting element

The completion of these goals requires the design of antenna-in-plasma codes which simulate the interaction of radiating antennas and the magnetized plasma in which they are immersed. Different codes have been developed that solve various aspects of the coupling problem and that are tailored to the particular physics in the corresponding region of the coupling environment.

# 1   Introduction

The primary focus of our research effort under AFOSR sponsorship has been the development of software for the purpose of studying the coupling of antennas to a magnetized plasma for application in the remediation of energetic electrons from the Van Allen radiation belts through in-situ VLF wave injection. As a direct result of this research, we have developed time and frequency domain codes for this purpose in order to gain insight into the complex nature of the physical processes inherent when using dipole antennas in a magnetized plasma operating at VLF frequencies.

Electric dipole antennas are commonly used in space plasmas with applications that range from radio frequency probing of the magnetosphere to plasma diagnostics [Carpenter and Anderson, 1992, Carpenter et al., 2003, Bell et al., 2004, Platino et al., 2005]. With the recent interest in the use of these antennas for the purpose of radiation belt remediation (RBR) [Inan et al., 2003], the characterization of the antenna-plasma coupling behavior in this regime is of primary importance. Along with ground based transmitters and naturally occurring sources of VLF radiation such as lightning and chorus [Abel and Thorne, 1998], it has been shown that in-situ injection of VLF electromagnetic waves can substantially reduce population lifetimes of highly energetic electrons in the Earths radiation belts. The dominant mechanism behind the precipitation of these energetic particles is pitch angle diffusion via cyclotron resonant wave-particle interactions [Albert, 2001].

Over the past five decades, there has been significant interest in the study of antenna-plasma interactions. Some of the first work in the field was performed

by Balmain [1964] who analytically determined the input impedance of electrically short dipole antennas using a quasi-electrostatic approach in a collisional ionospheric plasma. Subsequent review papers by Balmain [1972, 1979], extended this analysis to a variety of antennas operating in both isotropic and anisotropic plasmas including resonance and nonlinear effects. At roughly the same time Wang and Bell [1969, 1970, 1972c,a,b] derived closed-form expressions for the terminal properties and radiation characteristics of both dipole and loop antennas operating at ELF/VLF using a fully electromagnetic approach. Early theoretical work often made simplifying assumptions in order to provide analytical solutions such as a triangular current distribution on the antenna and a homogeneous linearized cold/warm plasma environment.

Whether operating as transmitting or receiving elements, electric dipole antennas will be surrounded by an electrostatic sheath which can significantly alter the antenna properties (both near and far field) relative to its freespace equivalent. For receiving purposes, the sheath will be on the order of a few Debye lengths and is well approximated by existing analytical theory. However, when used for applications requiring the application of large potentials to the transmitting element far in excess of the surrounding plasma potential, the sheath is highly nonlinear and its structure is unknown.

The emphasis of this report is on the near field properties of dipole antennas including the nonlinear effects of the sheath. This paper proceeds with a theoretical background outlining the various models used for simulating antenna-plasma interactions. We begin with the most simplified approach constituting a linearized plasma-fluid development coupled with Maxwell's equations in order to determine the impedance and current distribution on dipole antennas in the absence of the sheath. Then we increase the complexity of our model by including finite temperature and nonlinear effects by extending the number of fluid moments in our approach in order to determine the effects of the sheath on the near field properties of dipole antennas. The terminal properties of dipole antennas for the aforementioned cases are provided and a discussion of the relative importance of various fluid quantities in time-varying sheath formation is given.

# 2   Theoretical Development

Our plasma formulation uses a macroscopic multi-fluid approach to solve for the coupling between dipole antennas and the plasma in which they operate. The fluid model is comprised of moments of the Vlasov equation for each particle species representing the time-evolution of the particle distribution function $f = f(\mathbf{r}, \mathbf{v}, t)$ in a collisionless plasma where $\mathbf{r}$, $\mathbf{v}$ and $t$ are coordinates in configuration space, velocity space and time respectively. The Vlasov equation given by Equation 1.

$$\frac{\partial f}{\partial t} + (\mathbf{v} \cdot \nabla_{\mathbf{r}})f + \left[\frac{F}{m} \cdot \nabla_{\mathbf{v}}\right] f = 0 \qquad (1)$$

where $m$ is the particle mass, and $F = q(\mathbf{E} + v \times \mathbf{B})$ is the Lorentz force with charge $q$, electric field $\mathbf{E}$, and magnetic field $\mathbf{B}$. Since the bulk of the plasma between $L = 2$ and $L = 3$ is virtually cold ($\sim 2000°$) consisting of very low energy particles [Bezrukikh et al., 2003] we assume our initial distribution for each species is a Maxwellian distribution as in Calder and Laframboise [1990], Calder et al. [1993] and given by Equation 2 in a three-dimensional Cartesian coordinate system.

$$f = N_o \left(\frac{m}{2\pi kT}\right)^{\frac{3}{2}} e^{-\frac{m\mathbf{v}^2}{2kT}} \qquad (2)$$

$$\mathbf{v} = \left[(v_{\mathrm{x}} - v_{x0})(v_{\mathrm{y}} - v_{y0})(v_{\mathrm{z}} - v_{z0})\right]$$

where $N_o$ is the bulk density, $\mathbf{v} = \mathbf{v}(v_{\mathrm{x}}, v_{\mathrm{y}}, v_{\mathrm{z}})$ is the velocity vector represented by coordinates $v_{\mathrm{x}}$, $v_{\mathrm{y}}$ and $v_{\mathrm{z}}$ in velocity space, $v_{x0}$, $v_{y0}$ and $v_{z0}$ are the drift velocities in each respective direction, $k$ is Boltzmann's constant, and $T$ is temperature. In our simulations, we assume that the drift velocities $v_{x0}$, $v_{y0}$ and $v_{z0}$ are initially zero.

## 2.1   Moments of Vlasov Equation

The series of moments that comprise our fluid model are derived by integrating the Vlasov equation over velocity space in powers of $\mathbf{v}^{\mathrm{n}}$ where $n$ is the order of the moment. In many cases including ours, it is convenient to define the second and third order moments which specify the stress tensor $\mathbf{\Pi}$ and energy flux density $\mathcal{E}$ in the rest frame of the species using the relation $\mathbf{c} = \mathbf{v} - \mathbf{u}$ where $\mathbf{c}$ is the random velocity due to the thermal motions of the particles, $\mathbf{u}$ is the flow velocity, and $\mathbf{v}$ defines the velocity distribution of the particles in phase space as mentioned earlier. In the rest frame, $\mathbf{\Pi}$ and $\mathcal{E}$ become the pressure $\mathbf{P}$ and heat flux density $\mathbf{Q}$ which are

integrated with respect to the Vlasov equation in powers of $[\mathbf{v} - \mathbf{u}]^n$. The quantities comprising the first four moments given by Equations 3a-3d which are found in Chust and Belmont [2006] correspond to density, momentum, pressure, and heat-flux respectively and are repeated here for convenience.

$$\partial_t(nm) + \nabla \cdot (nm\mathbf{u}) = 0 \tag{3a}$$
$$\partial_t(nm\mathbf{u}) + \nabla \cdot (nm\mathbf{u}\mathbf{u} + \mathbf{P}) + S_m = 0 \tag{3b}$$
$$\partial_t(\mathbf{P}) + \nabla \cdot (\mathbf{u}\mathbf{P} + \mathbf{Q}) + S_P = 0 \tag{3c}$$
$$\partial_t(\mathbf{Q}) + \nabla \cdot (\mathbf{v}\mathbf{Q} + \mathbf{R}) + S_Q = 0 \tag{3d}$$

$$S_m = -nq\left(\mathbf{E} + \mathbf{u} \times \mathbf{B}\right)$$
$$S_p = \{\mathbf{P} \cdot \nabla(\mathbf{u}) + \Omega_c \times \mathbf{P}\}^{sym}$$
$$S_Q = \{\mathbf{Q} \cdot \nabla(\mathbf{u})\Omega_c \times \mathbf{Q} - \mathbf{P}\nabla \cdot (\mathbf{P})\frac{1}{nm}\}^{sym}$$

In Equations 3c and 3d, $\Omega_c$ represents the gyrofrequency vector along the magnetic field, $\mathbf{R}$ is the $4^{th}$ order moment, and the $sym$ symbolizes a symmetric tensor. It is useful to note that with each moment, the rank of each tensor increases by $x^n$ where $x$ is the number of dimensions and $n$ is the order of the moment, Therefore, the density equation for each species comprises only a single element while the heat-flux density tensor which is of rank three consists of 27 individual components. This can quickly render the fluid method intractable unless simplifying assumptions are made for higher moments.

We will compare three different fluid closure relations in this paper for simulating the coupling of the antenna to the plasma. The first is the cold plasma approximation in which we assume that the pressure tensor $\mathbf{P}$ is zero in the momentum transport equation. We also assume small scale perturbations in each of the conserved quantities such that Equations 3a-3b can be linearized and combined into a single equation for the current for each species given by Equation 4.

$$\frac{d\vec{J}_\alpha}{dt} + \nu_\alpha\vec{J}_\alpha = \frac{q_\alpha}{m_\alpha}\left(q_\alpha n_\alpha\vec{E} + \vec{J}_\alpha \times \vec{B}_o\right) \tag{4}$$

where $\vec{E}$ is the *electric* field, $J$, $\nu$, $n$, $q$, and $m$ are the *current density, collision frequency, number density, charge*, and *mass* of species $\alpha$ and $\vec{B}$ is the background magnetic field. Equation 4 represents a simplified version of the generalized Ohm's Law.

The second closure relation is the isothermal approx-

imation which provides a relationship between temperature and pressure given by $P = nkT$. This is the equation of state based on the ideal gas law for thermodynamics and provides a mechanism for truncating the set of infinite moments at the momentum equation assuming a diagonal pressure tensor and for the case in which the temperatures parallel and perpendicular to the magnetic field are the same, simplifies to an isotropic pressure. The third closure relation utilizes the assumption of adiabadicity $\nabla \cdot \mathbf{Q} = 0$ which essentially means that the contribution due to the heat-flux is negligible. However, in this case, all components of the pressure tensor are kept in the fluid description. This assumption as with all other closure relations given assumes that the distribution function remains sufficiently compact about the mean (thermal velocity) so that the first few moments provide an adequate description of the distribution. In fact, up until the addition of the heat-flux moment which allows for skew about the mean velocity in the distribution, all other moments assume a symmetry about the mean velocity. In the Results sections, we will compare via simulation various truncation relations for both magnetized and unmagnetized plasmas with respect to sheath formation, whereas Chust and Belmont [2006] provide a more analytical justification based on various time and spatial scales for the various truncation mechanisms without specifically addressing sheath dynamics.

In our initial cold plasma simulation work, the field quantities are solved for using Maxwell's equations given by Equations 5a - 5b.

$$\nabla \times \vec{H} = \sum_N \vec{J}_\alpha + \epsilon_o \frac{d\vec{E}}{dt} \tag{5a}$$

$$\nabla \times \vec{E} = -\mu_o \frac{d\vec{H}}{dt} \tag{5b}$$

where $\vec{E}$ and $\vec{H}$ are the wave *electric* and *magnetic* fields and $\vec{J}$ is the auxiliary current defined in Equation 4. As we will show in the Cold Plasma Results section, the current distribution is triangular for all cases shown using the fully electromagnetic model. With the inclusion of additional moments defining the warm plasma model in order to study sheath dynamics, we utilize Poisson's equation in order to ease the computational burden. Poisson's equation is given by:

3

$$\nabla \cdot \vec{E} = \frac{\sum\limits_{\alpha} \rho_\alpha}{\epsilon_o} \qquad (6)$$

where $\epsilon_o$ is the permittivity of free space, and the charge density $\rho$ is summed across all species $\alpha$ where $\alpha = 2$ representing only electrons and protons in our model. The use of Poisson's equation is fully justified since the sheath is primarily electrostatic in character and the use of Poisson's equation enforces a triangular current distribution across the antenna elements which we will show is consistent with our cold plasma results.

# 3   Cold Plasma Results

We now present results for the current distributions and input impedance of electric dipole antennas in a magnetized plasma. Finite Difference Frequency Domain (FDFD) simulations are carried out for dipole antennas oriented perpendicular with respect to the ambient static magnetic field. This orientation is chosen since the antenna pattern and power delivery are optimal for launching waves parallel to the static magnetic field Wang and Bell [1972c,a]. Antennas considered for the purpose of our application are on the order of 100 m in length and up to 20 cm in diameter.

The FDFD method is well suited to model small geometries with respect to a free space wavelength. The antenna itself is assumed to be a PEC (Perfect Electric Conductor) and the current distribution along the length of the antenna is calculated by taking a line integral of the frequency domain magnetic field components encircling each wire element along the length of the antenna. The input impedance is calculated using:

$$Z_{\text{in}} = \frac{V(f)}{I(f)} = \frac{(\int \vec{E} \cdot dl)_{feed}}{(\oint \vec{H} \cdot dl)_{feed}} \qquad (7)$$

where the field quantities are already in the frequency domain per use of the FDFD method. (7) represents the ratio of the complex phasors quantities for the current and voltage at the terminals of the antenna.

For the purposes of our simulation, we first examine the properties of a 100 m long electric dipole antenna in a cold magnetized plasma operating near $L = 2$ in the magnetic equatorial plane. We consider an electron-proton plasma with $f_{pe} = 586$ kHz and $f_{ce} = 110$ kHz in a collisionless environment. The $\hat{z}$ directed antenna

is located in the center of the space and is 20 cm in diameter which corresponds to the smallest cell size in the space. The magnetic field is oriented in the $+\hat{y}$ direction and a perfectly matched layer (PML) boundary condition is used to truncate the space in all directions. The dipole antenna is excited with an $\vec{E}_z$ hard source in the gap between the conducting elements with a value of 1 V/m and the system is allowed to converge with a relative residual norm of $10^{-6}$.

One of the primary benefits of using frequency over time domain analysis is the ability to use a different mesh and PML configuration for each simulation run. Though we do not use this advantage to the full extent available (a different configuration for each frequency), we do use a different mesh and PML configuration for frequencies below and above $f_{\text{LHR}}$ for which the propagation characteristics are quite different as shown in Figures 1 and 2.
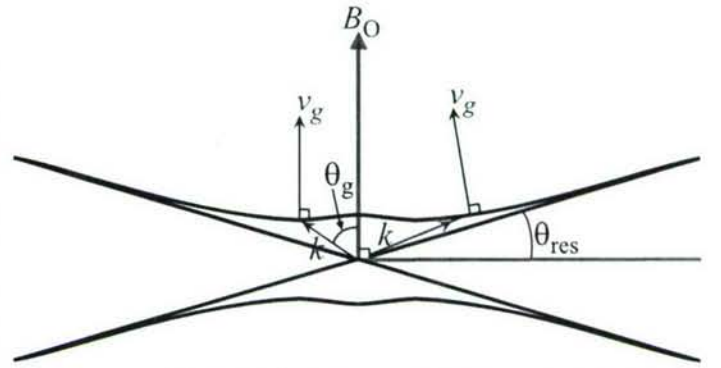


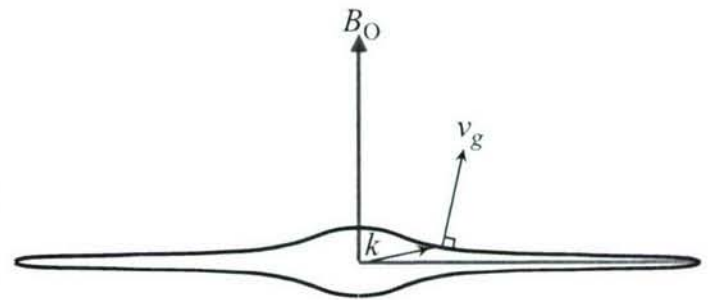Figure 1: Refractive index surface for $f_{\text{LHR}} < f < f_{ce}/2$.



Figure 2: Refractive index surface for $f_{ci} \ll f < f_{\text{LHR}}$.

In Figures 1 and 2, $\vec{k}$ represents the wave number, $\vec{v}_g$ is the group velocity or velocity of energy flow given by the normal to the refractive index surface, and $\theta_{\text{res}}$ is the resonance cone angle at which the refractive index tends to infinity. The refractive index surfaces depicted in Figures 1 and 2 are functions of the wave normal angle,

4

defined as the angle between the $\vec{k}$-vector direction and the ambient magnetic field. The Gendrin angle is the non-zero wave normal angle at which the group velocity is parallel with the static magnetic field Gendrin [1961]. The Gendrin angle $\theta_g$ is illustrated in Figure 1 and for high ratios of $\frac{f_{pe}}{f_{ce}}$ is given approximately by the relation Gendrin [1961]:

$$\cos\theta_g \approx \frac{2\omega}{\omega_{ce}}, \tag{8}$$

where $\omega$ and $\omega_{ce}$ are the angular wave frequency and electron gyrofrequencies respectively.

For frequencies $f > f_{\mathrm{LHR}}$, there exists a range of $\hat{k}$-vectors for which the refractive index is very large and tending to infinity at the resonance cone angle $\theta_{\mathrm{res}}$ as shown in Figure 1. It is therefore imperative to utilize much smaller cells in order to capture these tiny wavelengths resulting from the high refractive index relative to those used for frequencies $f < f_{\mathrm{LHR}}$. For frequencies below $f_{\mathrm{LHR}}$, the resonance cone disappears as shown in Figure 2 with the refractive index surface being closed and possessing a maximum of $n \approx 600$ at directions orthogonal to the background magnetic field. The refractive index surface for $f < f_{\mathrm{LHR}}$ becomes more isotropic with decreasing frequency and thus larger cells sizes may be used.

As stated previously, the computational space is truncated using a PML absorbing boundary condition (ABC) Berenger [1994]. As with the computational mesh, the PML configuration is different for frequencies above and below $f_{\mathrm{LHR}}$. For frequencies $f > f_{\mathrm{LHR}}$, the PML consists of 10 cells in the $\hat{x}$ direction, 15 cells in the $\hat{y}$ direction, and 10 cells in the $\hat{z}$ direction. The PML layers in both the $\hat{x}$ and $\hat{z}$ directions are made to absorb only evanescent waves, while the PML layers in the $\hat{y}$ direction absorb both propagating and evanescent waves in this frequency range. For frequencies below $f_{\mathrm{LHR}}$, there are 10 PML layers in all directions and each PML is made to absorb both propagating and evanescent waves. The PML parameters are different for frequencies above and below $f_{\mathrm{LHR}}$ since the cell sizes and refractive index surfaces are quite different in the two cases. The PML performance up to 10 kHz including frequencies above and below $f_{\mathrm{LHR}}$ for the simulations in the $L = 2$ environment are shown in Figures 3 and 4 corresponding to PML orientations parallel and perpendicular to the static magnetic field respectively.
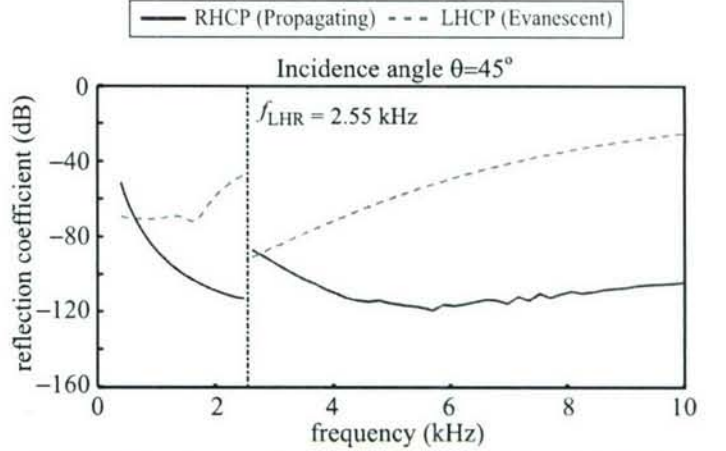


Figure 3: Reflection coefficient calculations for PML oriented along $\hat{y}$-direction, parallel to the static magnetic field, for an angle of $45°$ with respect to normal incidence.
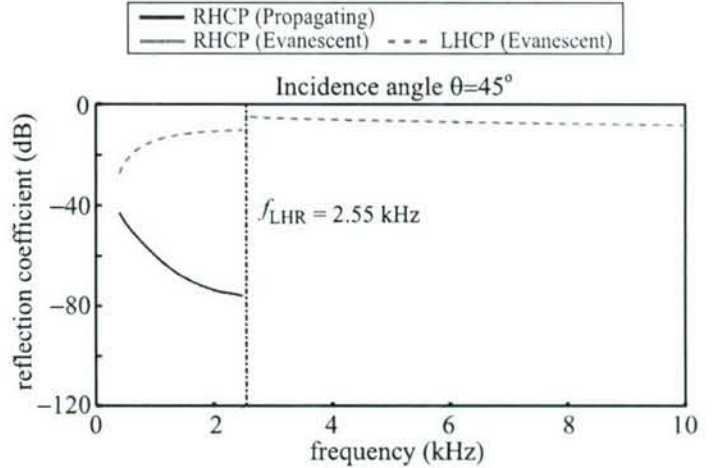


Figure 4: Reflection coefficient calculations for PML oriented in $\hat{x}$ and $\hat{z}$-directions, perpendicular to the static magnetic field, for an angle of $45°$ with respect to normal incidence.

There are several things to notice about the plots of Figures 3 and 4. First of all, the only propagating modes in the frequency range $f_{ci} \ll f < f_{ce}$ where $f_{ci} \ll f_{\mathrm{LHR}}$ are right-hand circularly-polarized (RHCP). All waves launched from the antenna that are left-hand circularly-polarized (LHCP) are evanescent in the plasma at these frequencies. The discontinuity in the reflection coefficient calculations at $f_{\mathrm{LHR}}$ is a direct result of the differences in mesh and PML geometries across this transition region as stated earlier. Though the PML performance for LHCP waves representing the directions orthogonal to the static magnetic field described by Figure 4 is relatively poor, these waves will reflect into the PML parallel to the static magnetic field of Figure 3 and be

5

absorbed with greater attenuation. The PML in the direction orthogonal to the static magnetic field as represented in Figure 4 for frequencies $f > f_{LHR}$ has been tailored to absorb evanescent waves only to avoid the PML instabilities mentioned earlier. As a result, the incident RHCP propagating modes experience no attenuation and are perfectly reflected. Finally, for small incident angles, the RHCP wave incident upon the PML is evanescent. The resonance cone angle of Figure 1 is $5°$ at $\approx 9.2$ kHz and marks the point at which the incident RHCP waves become evanescent and able to be absorbed by this PML.

## 3.1 Current Distributions and Input Impedance Calculations for a 100 m Antenna at $L = 2$

The first case study is a 100 m antenna located in the equatorial plane at $L = 2$. We compare the current distributions for frequencies above and below the local LHR frequency which is $f_{LHR} = 2.55$ kHz. Figures 5 and 6 represent the current distributions for two frequencies below $f_{LHR}$.



Figure 6: $L = 2$ **Current distribution for a 100 m antenna at f = 2.0 kHz driving frequency.**

It can be seen from Figures 5 and 6 that the current distributions are virtually identical to the assumed triangular distribution of Wang and Bell [1969, 1970], Wang [1970]. One important point is that for a simulated antenna of finite thickness, the current is non-zero at the ends, contrary to the ideal case, since the finite area allows for a build up of charge at the tips. The simulation results thus reflect this realistic condition much better than the idealized case shown in dashed lines. Figures 7 and 8 represent the current distributions for two frequencies above $f_{LHR}$.
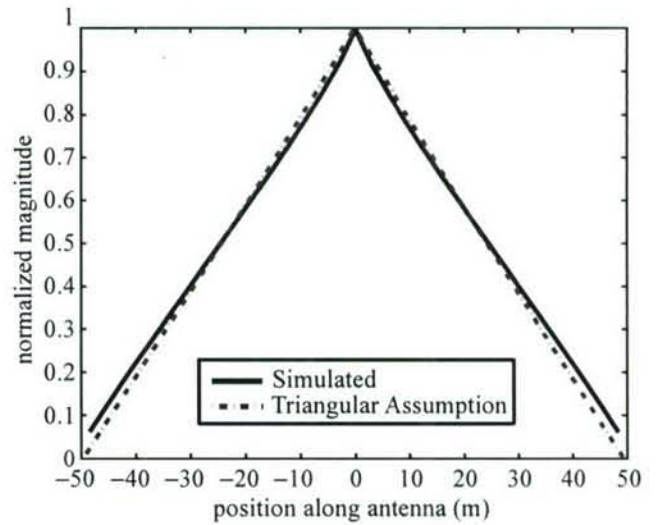


Figure 5: $L = 2$ **Current distribution for a 100 m antenna at f = 400 Hz driving frequency.**



Figure 7: $L = 2$ **Current distribution for a 100 m antenna at f = 2.6 kHz.**
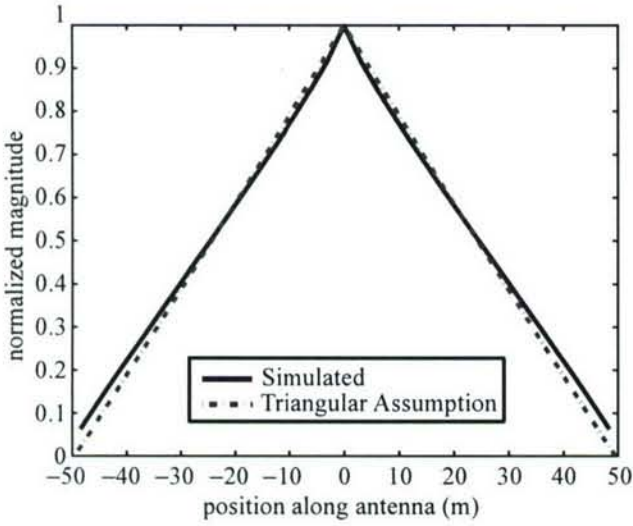
6

Figure 8: $L = 2$ **Current distribution for a 100 m antenna at f = 10.0 kHz.**

Once again, there is no significant deviation from the assumed triangular distribution, except for the realistic end-effect due to the finite antenna radius.

Figure 9 compares the simulated input impedance of the 100 m dipole antenna at $L = 2$ with results obtained from Wang and Bell [1969, 1970], Wang [1970].
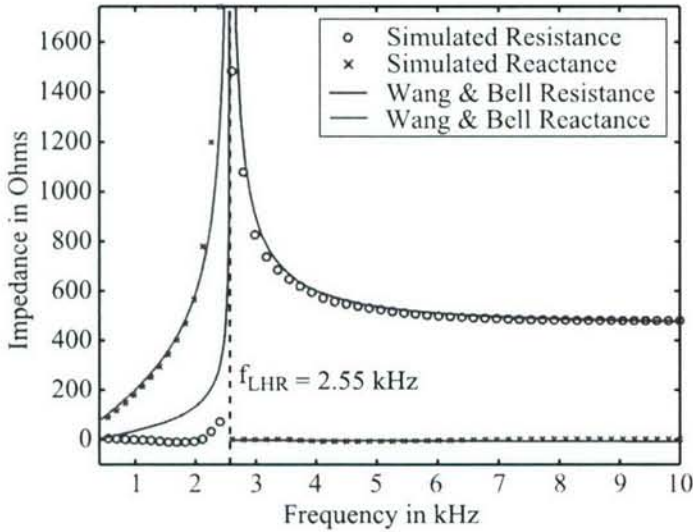


Figure 9: **Input impedance for a 100 m antenna at $L = 2$.**

The plots for both the resistance and reactance calculated with our numerical simulation are in good agreement with those evaluated analytically by Wang and Bell [1969, 1970], Wang [1970]. Below $f_{LHR}$, Wang and Bell [1969, 1970], Wang [1970], predict the reactance to vary

from approximately $100\Omega$ at zero frequency to $\infty$ at the LHR frequency. Unlike with the quasi-electrostatic assumption of Balmain [1964], the work of Wang and Bell [1969, 1970], Wang [1970] predict the resistance to have a non-zero value below the LHR frequency ranging from $0\Omega$ at zero frequency to $\infty$ at the LHR frequency. These trends are reflected in the simulated results as shown in Figure 9. Above $f_{LHR}$, the analytical reactance varies from $0\Omega$ to about $-8\Omega$ at 10 kHz. The simulated results in these regimes are within about $15\Omega$.

## 3.2 Current Distributions and Input Impedance Calculations for a 100 m Antenna at $L = 3$

The second cold plasma case study examines the properties of a 100 m antenna located at $L = 3$ in the equatorial plane. Typical values of the plasma and gyrofrequencies at $L = 3$ are $f_{pe} = 220$ kHz and $f_{ce} = 33$ kHz respectively. Since the PML performance characteristics of Figures 3 and 4 are very similar to the simulation setup at $L = 2$, these characteristics are not shown. Only two different examples of the current distribution are given since they are not markedly different than those for the cases of an antenna at $L = 2$. Figures 10 and 11 represent the current distributions for frequencies above and below $f_{LHR} = 761$ Hz.
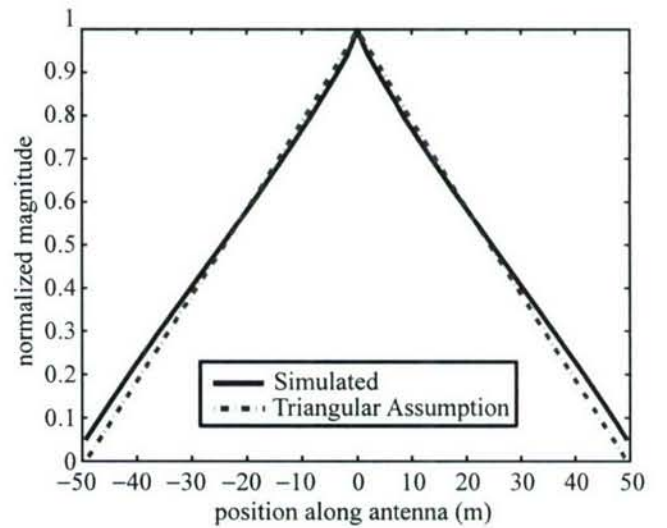


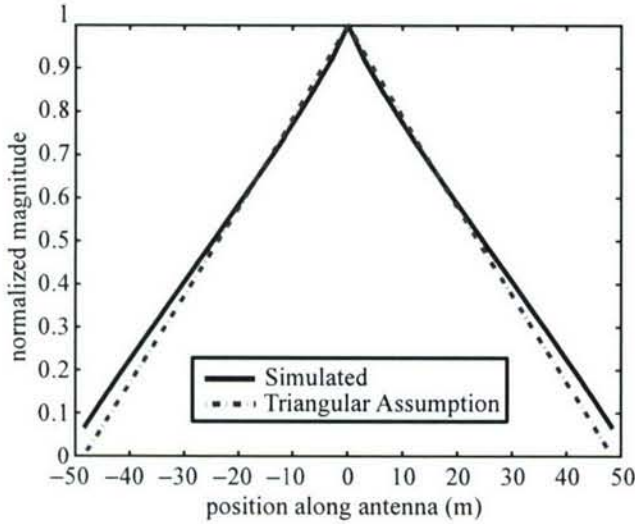Figure 10: $L = 3$ **Current distribution for a 100 m antenna at f=460 Hz driving frequency.**

7

**Figure 11:** $L = 3$ **Current distribution for a 100 m antenna at f=4.0 kHz driving frequency.**

It can be seen from Figures 10 and 11 that there is no significant deviation from a triangular current distribution for an antenna subject to a decrease in plasma and gyrofrequencies. Figure 12 compares the simulated input impedance of the 100 m dipole antenna at $L = 3$ with results obtained from Wang and Bell [1969, 1970], Wang [1970].
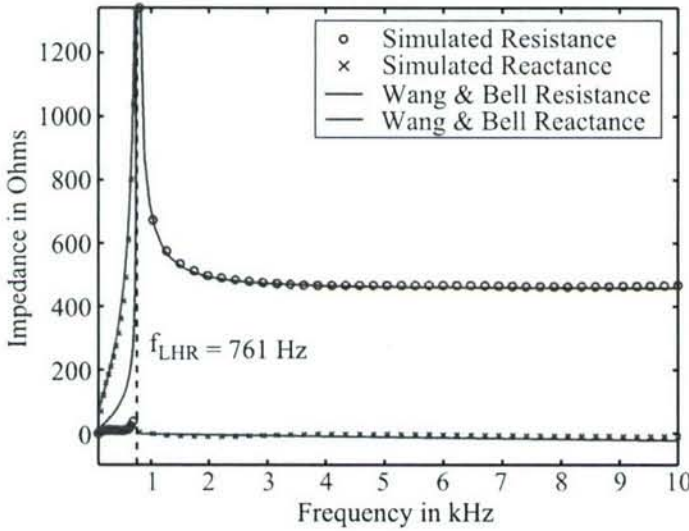


**Figure 12: Input impedance for a 100 m antenna at $L = 3$.**

As with the results from the previous case study, the impedance characteristics in Figure 12 exhibit very good agreement with the work of Wang and Bell [1969, 1970], Wang [1970]. Our results from this section validate our

model using the cold plasma approximation. In the next section, we extend the capability of the model through the addition of more moments to the fluid representation allowing for the formation of the sheath surrounding the antenna. In particular, we will examine the effects of the sheath on the impedance characteristics of the antenna.

# 4 Warm Plasma Results

The warm plasma fluid formulation allows for the study of the sheath formation surrounding an electric dipole antenna. We will show that it is the sheath which dominates the tuning properties of the antenna and it is thus imperative to accurately simulate its contribution to the overall antenna-plasma coupling response. In this section, we will examine the effects of two various closure mechanisms in the context of 2-dimensional simulations and then analyze the sheath surrounding an electric dipole antenna in 3-dimensions.

## 4.1 Closure Relations

In the warm fluid approximation, no assumptions of linearity are made and thus all convective terms in the system of moments defined by Equations 3a-3d are preserved. Two warm plasma closure mechanisms are considered in this report. The first closure relation is the isothermal approximation which assumes that the pressure tensor is diagonal and given by the ideal gas law relation discussed earlier. In this approximation, the system of equations representing the plasma is given by the first two fluid moments given by Equations 3a-3b.

The second closure relation assumes that the system is adiabatic $\nabla \cdot \mathbf{Q} = 0$ and thus all terms involving the heat flux tensor are zero. In this formulation, the plasma is represented by the first three moments of Equation 1 given by Equations 3a-3c.

## 4.2 Two-dimensional Simulation

The first study considered is that of a two dimensional infinite line source in an isotropic plasma with parameters corresponding to $L = 2$. We use an artificial ion-electron mass ratio of $\frac{m_i}{m_e} = 200$ which is a commonly used practice in order to ease the computation burden [Calder et al., 1993]. The simulation uses Neumann boundary conditions for the fluid at the edge of the space and any

particles hitting the line source are completely absorbed. A plot of the simulation domain is shown in Figure 13.
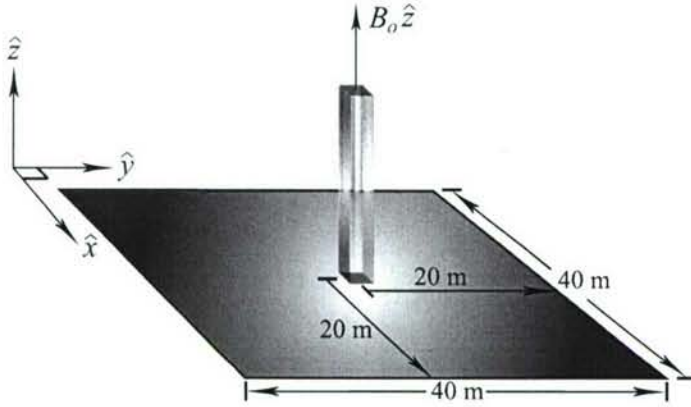


Figure 13: 2-dimensional computational domain.

We examine the time-varying sheath formation using a quasi-electrostatic approach as discussed earlier. This involves the use of Poisson's equation in which a sinusoidal potential is applied to the line element with a peak potential of approximately 100V. In order to determine the importance of the proton dynamics in sheath formation, we consider RF frequencies above and below the proton plasma frequency. Since the plasma is isotropic in our 2-d case, we take a vertical slice plane through the line element and plot the resulting potential and density profiles using a 1-d representation. A diagram of the slice plane is shown in Figure 14.
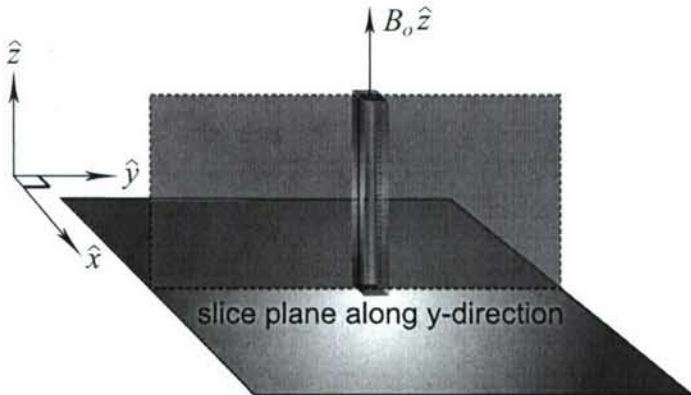


Figure 14: Slice plane through infinite line source.

As the potential becomes positive, the protons are pushed away from the antenna while the electrons are collected, while during the negative cycle, the opposite occurs with the protons being collected and the electrons being repelled from the line element. Figures 15

and 16 show the potential and density profiles for the electrons and protons of our two species plasma after a number of periods of the 25kHz applied potential (5kHz above the proton plasma frequency) by which time the response is periodic.
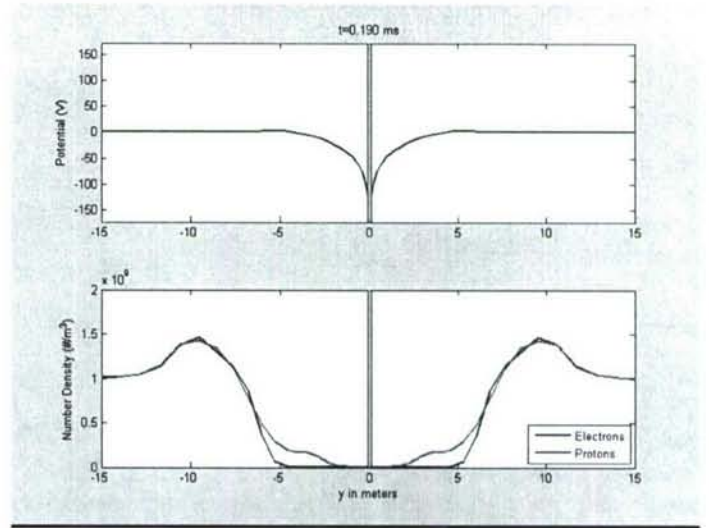


Figure 15: Snapshot during negative potential cycle of infinite line source.
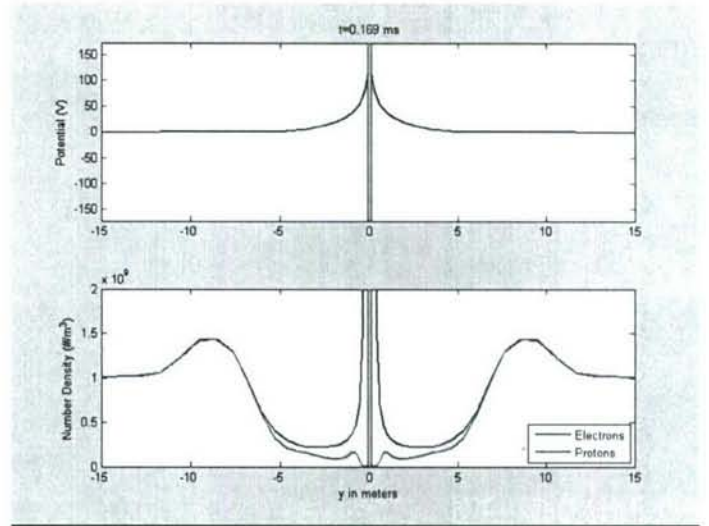


Figure 16: Snapshot during positive potential cycle of infinite line source.

During the start of the initial transient response, the protons are pushed away from the line source and due to their inertia, are never pulled back during the opposite cycle. This forms a permanent evacuated region of protons with the only substantial current collection on the line element being due to the electron response.

9

This behavior is in disagreement with previous analytical works in which the proton motion was neglected since it was thought that the much heaver mass of the protons would essentially make them immobile [Mlodnosky and Garriott, 1963, Baker et al., 1973, Song et al., 2007].

Figures 17-20 represent the current collection on the line element for a given RF applied potential for frequencies above and below the proton plasma frequency. The blue curves represent the isothermal approximation (2-moments) and the red curves represent the adiabatic approximation (3-moments). The proton plasma frequency with the proton-electron mass ratio of 200 is approximately 20kHz.
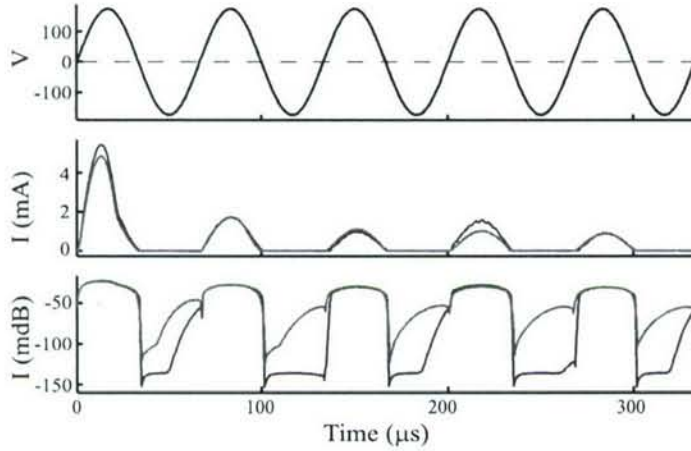


Figure 17: Current-voltage relationship for isotropic plasma with sinusoidal applied potential at 15kHz. 'Blue' - 2 moments. 'Red' - 3 moments.
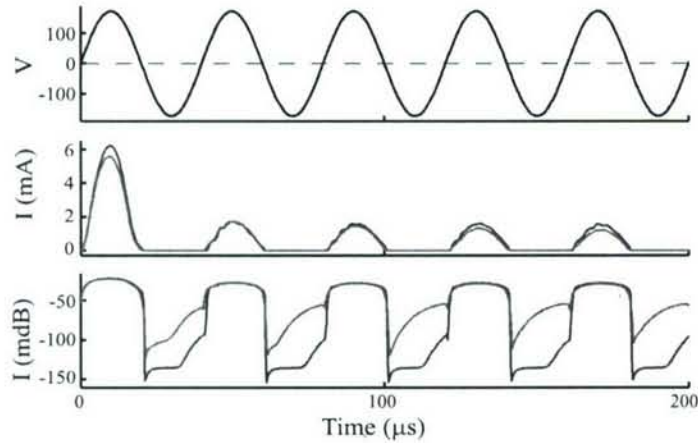


Figure 18: Current-voltage relationship for isotropic plasma with sinusoidal applied potential at 25kHz. 'Blue' - 2 moments. 'Red' - 3 moments.

Figures 17 and 18 represent the current collection on the line element assuming an isotropic plasma. The current waveform is shown in both linear and log scales in order to visualize the small contribution of the protons. Although the proton contribution to the current is negligible as seen per the diode type behavior, it is non-zero. The other important point is that there is little difference between the isothermal and adiabatic approximations suggesting that only a small number of moments are necessary in order to capture the relevant physics in sheath formation even under the collisionless assumption. This conclusion is supported by the earlier work of Thiemann et al. [1992] who compared both a 2-moment fluid code and a particle in cell (PIC) code with good qualitative agreement in a collisionless isotropic plasma.

Figures 19 and 20 include the effects of a static magnetic field oriented in the $\hat{z}$ direction as shown in Figure 13.
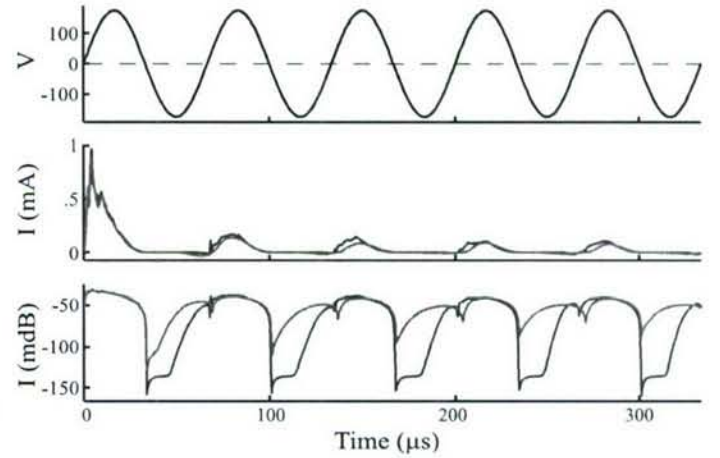


Figure 19: Current-voltage relationship for magnetized plasma with sinusoidal applied potential at 15kHz. 'Blue' - 2 moments. 'Red' - 3 moments.
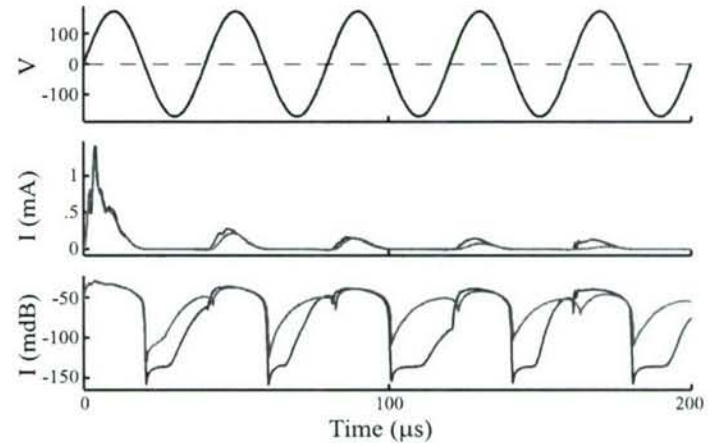


Figure 20: Current-voltage relationship for magnetized plasma with sinusoidal applied potential at 25kHz. 'Blue' - 2 moments. 'Red' - 3 moments.

The inclusion of the magnetic field in the formulation has the effect of limiting the current flow to the line element as expected since charged particles gyrate around magnetic field lines.

## 4.3  Three-dimensional Simulation

In this section we use our warm fluid code to examine the formation of the sheath surrounding a dipole antenna in a magnetized plasma in 3-dimensions. The dipole is 20 m in length, 10 cm in diameter, and possesses a 2 m gap between elements. We consider an electric dipole antenna operating in conditions corresponding to $L = 2$ and $L = 3$ in the geomagnetic equatorial plane excited with a maximum potential difference of approximately 100V. The same scaled proton-electron mass ratio is used as in the 2-dimensional simulations. Only perpendicular orientations with respect to the background magnetic field are considered as in the cold plasma simulation runs. Since there was virtually no difference in the behavior of the current collection for the 2-dimensional cases for frequencies just above and below the proton plasma frequency, all 3-d simulation runs are performed at the proton plasma frequency. We assume that an electron gun is present on board the spacecraft such that any particles hitting the antenna are completely absorbed and are assumed not to reverse bias the antenna.

The first case study is a dipole antenna at $L = 3$ where the magnetic field is not as strong and the Debye length is slightly smaller than the operating region at $L = 2$. A sketch of the simulation region is shown in Figure 21.
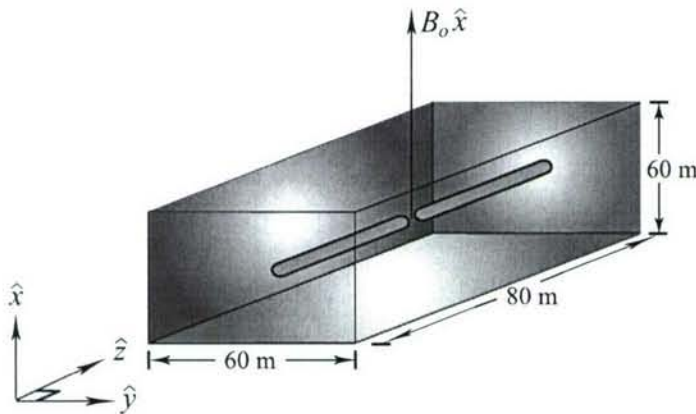
In this paper, we define the edge of the plasma sheath as the point at which the potential drops to within 10% of the maximum/minimum amplitude as shown in Figure 22.
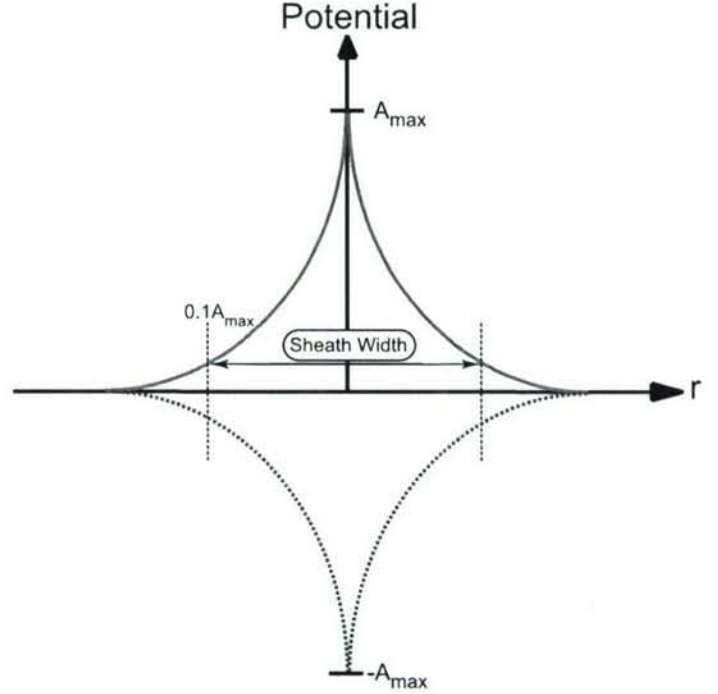


Figure 22: Diagram describing location of sheath edge.

Figure 23 represents and orthographic projection of the fully expanded sheath during the peak of the sinusoidal cycle after several periods in each slice plane. It can be seen from Figure 23 that the sheath is approximately 1 m wide at is virtually symmetric in each of the slice planes suggesting that the magnetic field does not play much of a role in the steady-state formation of the sheath. In addition, the sheaths on each element do not overlap meaning that both elements are electrically isolated from one another with no current flowing between them.
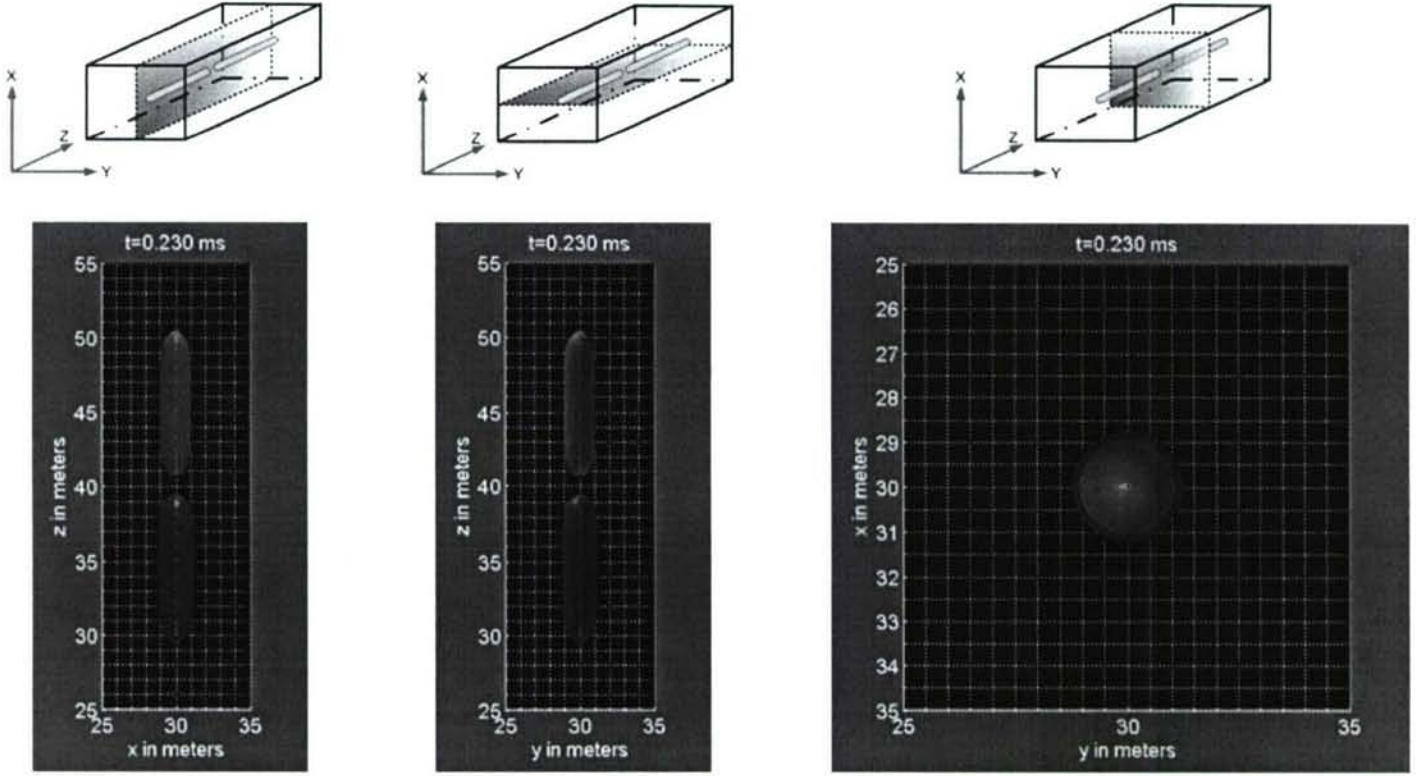


Figure 21: 3-dimensional computational domain at $L = 3$.

**Figure 23: Orthographic projection of expanded sheath for $L = 3$ at maximum potential difference 100V. Operating frequency is at $f = f_{pi}$.**

Figure 24 shows the time-domain impedance characteristics for the dipole antenna located at $L = 3$ including, potential, current, resistance and capacitance. The most notable feature of Figure 24 is that both the resistance and capacitance do not vary significantly over the RF cycle with the capacitance and resistance being roughly 10 pF and $10k\Omega$ respectively.
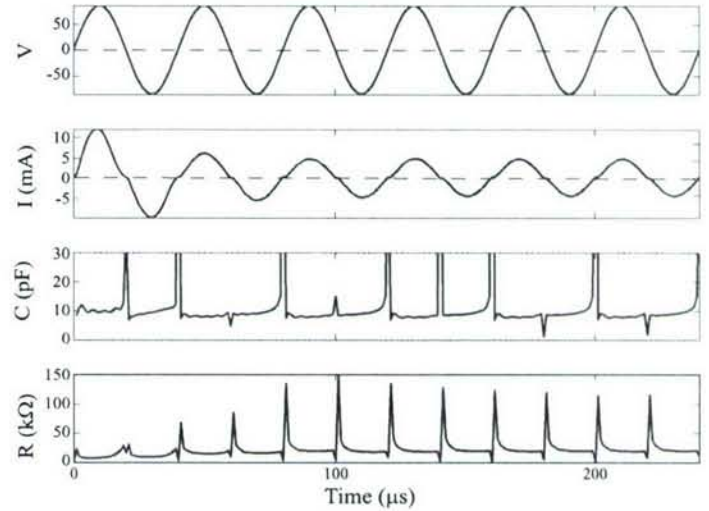


**Figure 24: Time-domain terminal characteristics for 20 m antenna located at $L = 3$.**

The final case study is a dipole antenna located at $L = 2$ where the magnetic field is more appreciable than that which exists at $L = 3$. Since the Debye length is smaller at $L = 2$, the computational domain is slightly smaller. A sketch of the simulation region is shown in
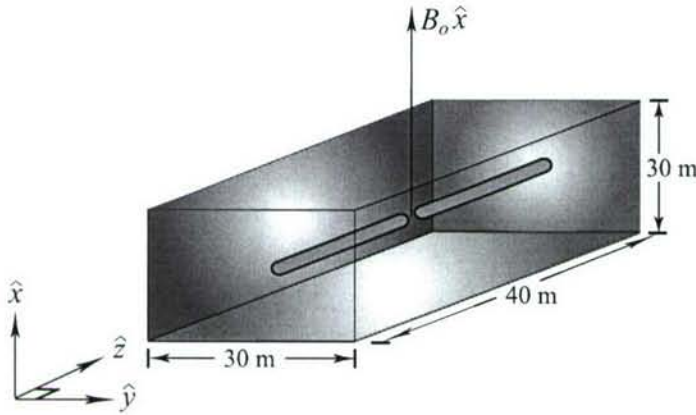
Figure 25.



Figure 25: 3-dimensional computational domain at $L = 2$.

Although not shown here, the only major difference between the runs at $L = 2$ and $L = 3$ is during the initial transient response in which the transient sheath expands along the field line. However the steady-state sheath (reached after a few sinusoid cycles) is virtually the same as that found at $L = 3$ with only a very slight increase in the amount of asymmetry along the slice planes. Figure 26 represents the corresponding orthographic projection of the fully expanded sheath for the case at $L = 2$.
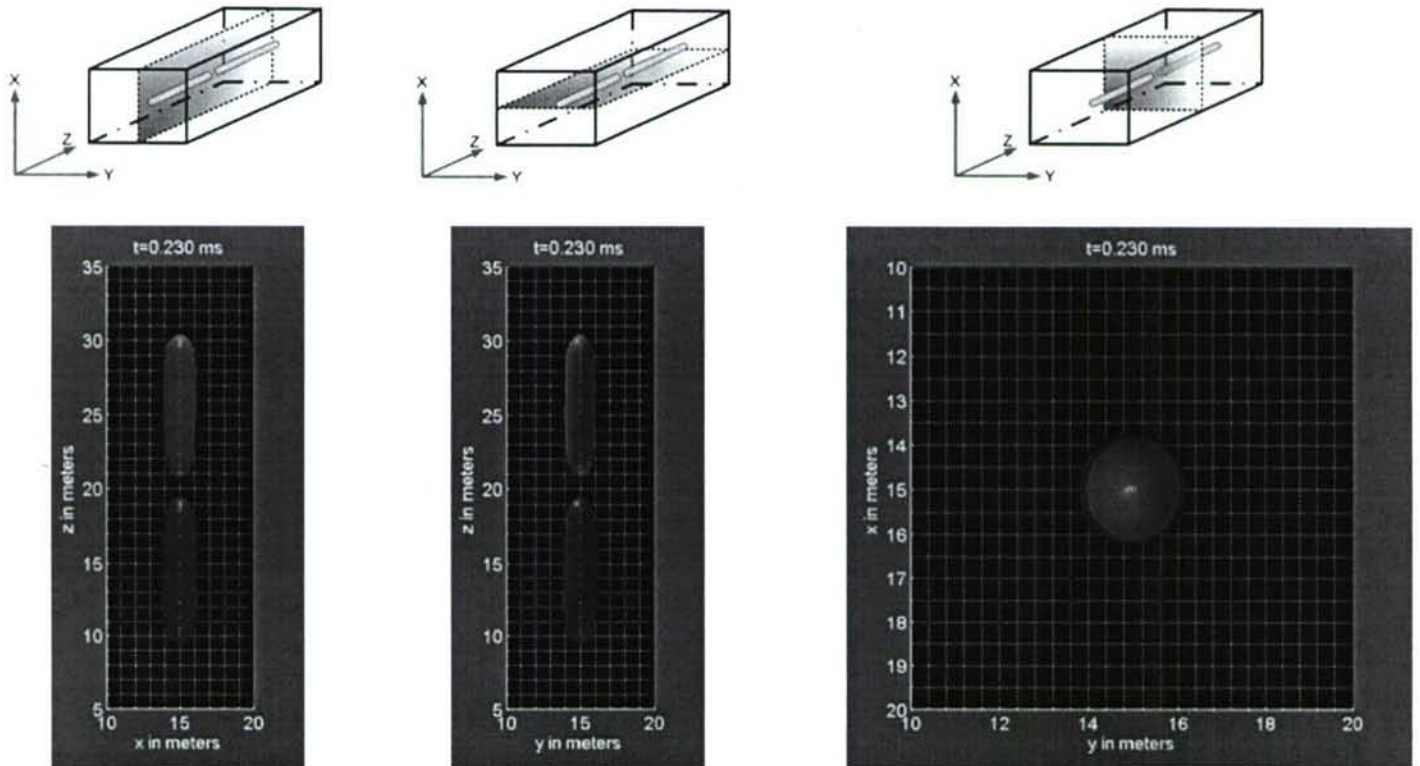


Figure 26: Orthographic projection of expanded sheath for $L = 2$ at maximum potential difference 100V. Operating frequency is at $f = f_{pi}$.

Figure 27 is a plot of the terminal properties for the antenna at $L = 2$ with similar agreement to the case study at $L = 3$.
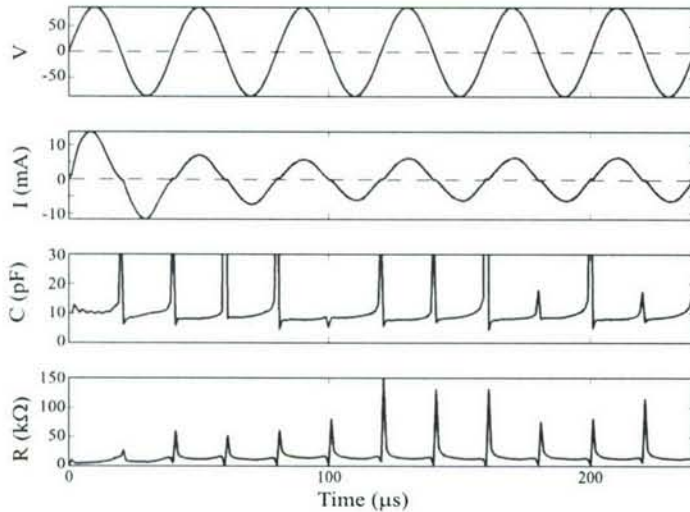
**Figure 27: Time-domain terminal characteristics for 20 m antenna located at $L = 2$.**

## 5 Discussion

This work constitutes a major achievement in the determination of the coupling behavior of antennas to a magnetoplasma using a multi step approach. The cold plasma model was the simplest approximation used and from the results we were able to obtain some insight into the coupling of dipole antennas to the surrounding plasma. From the cold plasma simulation results, we determined that the current distribution was triangular for the antenna parameters used which validates the assumption used in previous analytical work. Also, in the absence of the sheath, it was shown that for frequencies above the LHR frequency, the input impedance does not vary significantly as a function of frequency meaning that the antenna is self tuning and can be used over a broad frequency range. With the addition of the warm plasma fluid approximation, we gained the capability of examining the formation of the electrostatic sheath and were able to draw a number of conclusions based on these results. The first result is that sheath structure is periodic using a sinusoidal waveform excitation exhibiting a quasi-steady state structure. In addition, we have shown that the common assumption of immobile protons used in past work is incorrect with the density of protons varying significantly throughout the sheath region and contributing slightly to the current collection. Lastly, we have shown that not only does the sheath dominate the tuning properties of the antenna, but that the time-varying resistance and capacitance throughout the RF cycle do not vary by orders of magnitude (logarithmically) as suggested by previous authors [Mlodnosky and Garriott, 1963, Baker et al., 1973, Song et al., 2007].

## 6 Publications

Additional progress in the program has been reported in a number of publications as referenced below:

1. Bell, T., Inan, U., and Chevalier, T. (2006). Current distribution of a vlf electric dipole antenna in the plasmasphere. *Radio Science*, 41(2).

2. Chevalier, M., Chevalier, T., and Inan, U. (2006). A pml utilizing k-vector information as applied to the whistler mode in a magnetized plasma. *IEEE Antennas and Wireless Propagation Letters*, In Press.

3. Chevalier, T., Inan, U., and Bell, T. (2006). Terminal impedance and antenna current distribution of a vlf electric dipole in the inner magnetosphere. *Antennas and Propagation, IEEE Transactions on*, In Review.

## References

Abel, B. and Thorne, R. (1998). Electron scattering loss in earths inner magnetosphere. 1. dominant physical processes. *Journal of geophysical research*, 103(A2):2385–96.

Albert, J. (2001). Comparison of pitch angle diffusion by turbulent and monochromatic whistler waves. *Journal of geophysical research*, 106(A5):8477–82.

Baker, D., Weil, H., and Bearce, L. (1973). Impedance and large signal excitation of satellite-borne antennas in the ionosphere. *IEEE transactions on antennas and propagation*, AP-21(5):672–9.

Balmain, K. (1964). The Impedance of a Short Dipole Antenna in a Magnetoplasma. *IEEE transactions on antennas and propagation*, AP-12(5):605–617.

Balmain, K. (1972). Antennas in Plasma: Characteristics as Functions of Frequency. *Radio science*, 7(8-9):771–5.

Balmain, K. (1979). Properties of Antennas in Plasmas. *Annales des telecommunications*, 34(3-4):273–83.

Bell, T., Inan, U., Platino, M., Pickett, J., Kossey, P., and Kennedy, E. (2004). Cluster observations of lower hybrid waves excited at high altitudes by electromagnetic whistler mode signals from the haarp facility. *Geophysical research letters*, 31(6):L06811–5.

Berenger, J.-P. (1994). A Perfectly Matched Layer for the Absorption of Electromagnetic Waves. *Journal of Computational Physics*, 114(2):185–200.

Bezrukikh, V. V., Kotova, G. A., Lezhen, L. A., Lemaire, J., Pierrard, V., and Venediktov, Y. I. (2003). Dynamics of temperature and density of cold protons of the earths plasmasphere measured by the auroral probe/alpha-3 experiment data during geomagnetic disturbances. *Cosmic research*, 41(4):392.

Calder, A. C., Hulbert, G. W., and Laframboise, J. G. (1993). Sheath dynamics of electrodes stepped to large negative potentials. *Physics of fluids. B, Plasma physics*, 5(3):674.

Calder, A. C. and Laframboise, J. G. (1990). Time-dependent sheath response to abrupt electrode voltage changes. *Physics of fluids. B, Plasma physics*, 2(3):655.

Carpenter, D. and Anderson, R. (1992). An isee/whistler model of equatorial electron density in the magnetosphere. *Journal of geophysical research*, 97(A2):1097–108.

Carpenter, D., Bell, T., Inan, U., Benson, R., Sonwalkar, V., Reinisch, B., and Gallagher, D. (2003). Z-mode sounding within propagation cavities and other inner magnetospheric regions by the rpi instrument on the image satellite. *Journal of geophysical research*, 108(A12):SMP7–1.

Chust, T. and Belmont, G. (2006). Closure of fluid equations in collisionless magnetoplasmas. *Physics of Plasmas*, 13(1):012506.

Gendrin, R. (1961). Le guidage des whistlers par le champ magnetique. *Planetary and Space Science*, 5(4):274–278.

Inan, U., Bell, T., Bortnik, J., and Albert, J. (2003). Controlled precipitation of radiation belt electrons. *Journal of geophysical research*, 108(A5):1186–.

Mlodnosky, R. F. and Garriott, O. K. (1963). The v.l.f. admittance of a dipole in the lower ionosphere. *Proc. of the Int'l Conf. on the Ionosphere, London, July 1962*, page 484.

Platino, M., Inan, U., Bell, T., Gurnett, D., Pickett, J., Canu, P., and Decreau, P. (2005). Whistlers observed by the cluster spacecraft outside the plasmasphere. *Journal of geophysical research*, 110(A3):–.

Song, P., Reinisch, B. W., Paznukhov, V., Sales, G., Cooke, D., Tu, J. N., Huang, X., Bibl, K., and Galkin, I. (2007). High-voltage antenna-plasma interaction in whistler wave transmission: Plasma sheath effects. *Journal of geophysical research*, 112(A3):A03205.

Thiemann, H., Ma, T. Z., and Schunk, R. W. (1992). High voltage spheres in an unmagnetized plasma: Fluid and pic simulations. *Advances in Space Research*, 12(12):57–60.

Wang, T. and Bell, T. (1969). Radiation resistance of a short dipole immersed in a cold magnetoionic medium. *Radio Science*, 4:167–+.

Wang, T. and Bell, T. (1970). On VLF radiation resistance of an electric dipole in a cold magnetoplasma. *Radio science*, 5(3):605–10.

Wang, T. and Bell, T. (1972a). Electric dipole radiation at VLF in a uniform warm magneto-plasma. *Revue de physique appliquee*, 7(1):11–20.

Wang, T. and Bell, T. (1972b). Vlf/elf input impedance of an arbitrarily oriented loop antenna in a cold collisionless multicomponent magnetoplasma. *Antennas and Propagation, IEEE Transactions on [legacy, pre - 1988]*, 20(3):394–398.

Wang, T. and Bell, T. (1972c). VLF/ELF radiation patterns of arbitrarily oriented electric and magnetic dipoles in a cold lossless multicomponent magnetoplasma. *Journal of geophysical research*, 77:1174–89.

Wang, T. N.-C. (1970). *Vlf Input Impedance Characteristics of an Electric Antenna in a Magnetoplasma*. PhD thesis, Stanford University.